

Investigating the disk-corona relation in a blue AGN sample *

Jie-Ying Liu^{1,2} and Bi-Fang Liu¹

¹ National Astronomical Observatories / Yunnan Observatory, Chinese Academy of Sciences, Kunming 650011, China; *ljy0807@ynao.ac.cn*

² Graduate University of Chinese Academy of Sciences, Beijing 100049, China

Received 2009 March 19; accepted 2009 May 6

Abstract We compile a blue AGN sample from SDSS and investigate how the ratio of hard X-ray to bolometric luminosity depends on the Eddington ratio and black hole mass. Our sample comprises 240 radio-quiet Seyfert 1 galaxies and QSOs. We find that the fraction of hard X-ray luminosity ($\log(L_{2-10\text{ keV}}/L_{\text{bol}})$) decreases with an increase of the Eddington ratio. We also find that the fraction of hard X-ray luminosity is independent of the black hole mass for radio-quiet AGNs. The relation of $\log(L_{2-10\text{ keV}}/L_{\text{bol}})$ decreasing with increasing Eddington ratio indicates that X-ray bolometric correction is not a constant, from a larger sample supporting the results of Vasudevan & Fabian. We interpret our results by the disk corona evaporation/condensation model. In the frame work of this model, Compton cooling becomes efficient in cooling the corona at high accretion rates (in units of Eddington rate), leading to condensation of coronal gas to the disk. Consequently, the relative strength of the corona to the disk becomes weaker at higher Eddington ratios. Therefore, the fraction of hard X-ray emission to disk emission and hence to the bolometric emission is smaller at higher Eddington ratios. The independence of the fraction of hard X-ray luminosity with respect to the mass of the black hole can also be explained by the disk corona model since the coronal structure and luminosity (in units of Eddington luminosity) are independent of the mass of black holes.

Key words: accretion: accretion disks — galaxies: active — X-rays: galaxies

1 INTRODUCTION

Accretions onto supermassive black holes are the key processes that produce the spectral energy distribution in AGNs, including the Big Blue Bump, soft X-ray excess, Fe K α lines at 6.4 keV and the hard X-ray tail. These observed spectral properties indicate that the cold and hot gas coexist near the central supermassive black hole. According to commonly accepted theory, the optical/UV radiations are emitted from a geometrically thin and optically thick disk (i.e. the cold gas) (e.g., Shakura & Sunyaev 1973; Lynden-Bell & Pringle 1974), and the hard X-rays arise from hot optically thin and geometrically thick accretion flows, such as the disk corona (Haardt & Maraschi 1991, 1993; Nakamura & Osaki 1993; Svensson & Zdziarski 1994; Kawaguchi et al. 2001; Cao 2009) or advection-dominated accretion flows (ADAF) (e. g., Narayan & Yi 1994, 1995; Narayan et al. 1998).

The disk corona model was proposed to explain the observed X-ray emission in Cyg X-1 (Bisnovatyi-Kogan & Blinnikov 1976; Liang & Price 1977). The accretion in the corona is supplied with

* Supported by the National Natural Science Foundation of China.

material and energy through disk evaporation (e.g., Meyer & Meyer-Hofmeister 1994; Liu et al. 1999) or a magnetic process (e.g. Galeev et al. 1979; Stella & Rosner 1984; Liu et al. 2002a, 2003). In AGNs, a hot corona sandwiched by a disk is thought responsible for emitting the X-rays (e.g. Haardt & Maraschi 1991; Nakamura & Osaki 1993; Kawaguchi et al. 2001; Liu et al. 2002a, 2003). In the context of these studies, it is often assumed that a fraction (f) of accretion energy is released in the corona from the results of fits of individual AGN spectra. Questions arise as, is the fraction f dependent on the Eddington ratio and the black hole? How does the relative strength of the corona to the disk vary with the Eddington ratio and the black hole mass?

In this work, we attempt to investigate these issues by using observations. We compile a large blue AGN sample of 240 objects derived from Dong et al. 2008 (hereafter Dong08), in which the objects are selected from the Sloan Digital Sky Survey (SDSS) DR4 spectral data and they are less affected by dust extinction. We investigate the correlation between the coronal component and Eddington ratio. We show how the coronal luminosity fraction varies with the Eddington ratio and black hole mass for radio-quiet (RQ) AGNs. The results are compared with previous results of Wang et al. (2004) for a sample of 56 RQ AGNs observed by ASCA and Yang et al. (2007) for a combined sample from different observational satellites. Our aim is to study the physical relation between the disk and the corona.

The outline of the paper is the following. In Section 2, the black hole mass, and the optical and X-ray luminosities are calculated. In Section 3, the overall properties of the sample and the correlation analyses are presented. In Section 4, the statistical results are interpreted by the disk corona model. The discussion and conclusions are given in Sections 5 and 6, respectively.

2 THE SAMPLE AND DATA REDUCTION

Our sample is derived from a blue AGN sample in Dong08. These blue AGNs are selected from the Sloan Digital Sky Survey (SDSS) DR4 spectral data, including Seyfert 1 galaxies and QSOs. They are less affected by dust extinction. In order to investigate the relation between the disk and the corona, and whether and how the black hole mass and the Eddington ratio affect this relation, we select the objects by the following criteria:

- (1) The objects are detected or covered by the Faint Images of Radio Sky at Twenty Centimeters (FIRST) survey;
- (2) The X-ray flux is available;
- (3) Combining the radio with the optical data, we can determine the radio loudness and the RQ AGNs are selected.

According to the above criteria, we analyze the sample in Dong08. Given the upper limit to the radio flux, 404 AGNs are detected or covered by FIRST. After matching the ROSAT bright and faint SRC Catalog database (ROSAT-SRC) with a distance criterion between the optical and X-ray source of $\Delta \leq 60''$ (Voges et al. 1994), we obtain a sample containing 258 AGNs.

We use the radio-loudness definition (Ivezić et al. 2002) to divide RQ and radio-loud (RL) AGNs, that is,

$$R_i \equiv \log \left(\frac{F_{20\text{ cm}}}{F_i} \right) = 0.4(i - t), \quad (1)$$

where F_i and $F_{20\text{ cm}}$ are flux densities at the I -band and 20 cm respectively, i is the I -band magnitude, and $t = -2.5 \log(F_{20\text{ cm}}/3631 \text{ Jy})$. Objects with $R_i > 1$ are RL and objects with $R_i < 1$ are RQ. According to this definition, 240 (93%) objects in the sample are RQ and 18 (7%) objects are RL. We mainly analyze these 240 RQ objects in order to constrain the accretion mechanism.

The black hole mass, M_{BH} , is a fundamental parameter of AGNs. Different methods have been developed to estimate the black hole mass (Woo & Urry 2002 and references therein; Vestergaard & Peterson 2006), of which the reverberation mapping is the most widely used method (Peterson 1993; Peterson et al. 2004). In the reverberation mapping method, the distance of the broad line region (BLR) from the central black hole can be deduced from the time lag between continuum and emission lines. By

combining the distance with the measured emission line width, the black hole mass can be determined. In our sample, we take the FWHM ($H\beta$) as the circular velocity in BLR. The size/distance of the BLR is given by an empirical relation with the continuum luminosity at 5100 Å (Vestergaard & Peterson 2006). Thus, the mass of black holes for RQ AGNs can be estimated as

$$\log M_{\text{BH}}(H\beta) = \log \left\{ \left[\frac{\text{FWHM}(H\beta)}{1000 \text{ km s}^{-1}} \right]^2 \left[\frac{\lambda L_{\lambda}(5100 \text{ Å})}{10^{44} \text{ erg s}^{-1}} \right]^{0.5} \right\} + (6.91 \pm 0.02). \quad (2)$$

The bolometric luminosity of AGNs is approximately calculated from optical continuum luminosity, $L_{\text{bol}} \approx 9\lambda L_{\lambda}$ (5100 Å) (Elvis et al. 1994). The Eddington ratio ($L_{\text{bol}}/L_{\text{Edd}}$) is then calculated from the bolometric luminosity and black hole mass,

$$L_{\text{bol}}/L_{\text{Edd}} = 0.072 \frac{\lambda L_{\lambda}(5100 \text{ Å})}{10^{44} \text{ erg s}^{-1}} \left(\frac{M_{\text{BH}}}{10^8 M_{\odot}} \right)^{-1}, \quad (3)$$

where the Eddington luminosity is $L_{\text{Edd}} = 1.25 \times 10^{38} M_{\text{BH}}/M_{\odot}$ erg s⁻¹.

We get the X-ray flux densities from the count rates using the energy to counts conversion factor (ECF) for power-law spectra and Galactic absorption, where the power-law photon indices and the corresponding absorption column densities (N_{H}) are estimated from the two hardness ratios given by the ROSAT-SRC. With the integrated flux densities in 0.1–2.4 keV and power-law indices Γ , we deduce the monochromatic flux at 2 keV. After deriving the flux at 2 keV, we extrapolate X-ray flux (F_{int}) in the range from 2 keV to 10 keV by assuming a constant hard X-ray photon index, $\Gamma = 1.9$ (Pounds et al. 1990; Reeves & Turner 2000). The X-ray luminosity is then calculated by the standard luminosity–flux relation,

$$L = 4\pi d_{\text{L}}^2 F_{\text{int}} (1+z)^{-(1-\alpha)}, \quad (4)$$

where $\alpha = \Gamma - 1$ and d_{L} is the luminosity distance related to the redshift and cosmology model.

Throughout this paper, we adopt the cosmology model with $H_0 = 70 \text{ km s}^{-1} \text{ Mpc}^{-1}$, $\Omega_M = 0.3$, $\Omega_\Lambda = 0.7$. Our sample is listed in Table 1.

3 DATA ANALYSIS AND RESULTS

3.1 Properties of the Sample

Figure 1 shows the histogram of black hole masses and Eddington ratios in our sample. It can be seen that the mass of black holes covers a large range from 10^6 to $10^{10} M_{\odot}$. The center of the distribution of M_{BH} for the sources is greater than $10^7 M_{\odot}$. The histogram of the Eddington ratios of the sample shows that the Eddington ratios range from $10^{-2.5}$ to 1.0; most of the objects show a high accretion rate. If the accretion mode in AGNs is similar to that in black hole X-ray binaries, the high accretion rates of our sample indicate that the thin disk extends down to the innermost stable circular orbit. Hence, the hard X-rays arise from a disk corona rather than an ADAF.

3.2 Correlation Analysis and Results

We plot the ratio of X-ray luminosity to the bolometric luminosity vs. the mass of black holes and vs. the Eddington ratio for RQ sources in Figure 2. In the upper two panels, the vertical axis is the logarithm of the fraction of hard X-ray luminosity to bolometric luminosity ($\log(L_{2-10 \text{ keV}}/L_{\text{bol}})$), while in the lower panels, the vertical axis is logarithm of the fraction of soft X-ray luminosity (0.1–2.4 keV) to the bolometric luminosity. Comparing the upper and lower panels, one can see that the distribution trends are different for the soft X-ray and hard X-ray fractions.

We test the correlations between $\log(L_{2-10 \text{ keV}}/L_{\text{bol}})$ and $\log(M_{\text{BH}})$ and between $\log(L_{2-10 \text{ keV}}/L_{\text{bol}})$ and the Eddington ratio by the method of Spearman's rank correlation analysis (William et al. 1992). We calculate the Spearman's rank correlation coefficient (ρ) and the two-sided significance of

Table 1 Blue AGN Sample

Object SDSS (1)	z (2)	$\log(M_{\text{BH}})$ (M_{\odot}) (3)	$L_{\text{5100 \AA}}$ ($10^{44} \text{ erg s}^{-1}$) (4)	$F_{20 \text{ cm}}$ (mJy) (5)	R_i (6)	$\log(L_{0.1-2.4 \text{ keV}})$ (erg s^{-1}) (7)	$\log(L_{2-10 \text{ keV}})$ (erg s^{-1}) (8)
000710.01+005329.0	0.31620	9.13	3.85	1.44	0.55	44.949	44.238
000834.72+003156.1	0.26303	7.71	2.71	<1.00	0.43	44.665	42.915
000943.14–090839.1	0.20958	8.52	2.09	<1.00	0.21	44.057	43.225
001247.93–084700.4	0.22006	8.01	1.95	<1.00	0.21	44.629	43.965
004319.74+005115.3	0.30807	9.36	3.08	1.60	0.80	44.425	44.099
010226.31–003904.6	0.29421	7.92	9.63	<1.00	-0.10	45.012	43.656
011254.92+000313.0	0.23855	8.14	1.98	<1.00	0.42	44.398	43.816
014017.07–005003.0	0.33424	8.92	13.40	<1.00	0.06	45.232	44.927
014234.40–011417.3	0.24453	7.14	0.68	<1.00	0.69	44.078	44.060
015530.01–085704.0	0.16465	8.48	1.78	<1.00	-0.04	44.212	43.739
015910.04+010514.6	0.21716	8.08	1.99	<1.00	0.22	44.164	43.731
022347.48–083655.5	0.26077	7.52	0.97	1.04	0.81	44.330	43.631
022417.16–092549.3	0.31148	8.79	1.72	<1.00	0.67	44.751	43.763
072937.04+375435.0	0.20364	7.23	1.39	<1.00	0.40	44.558	43.179
073503.49+431153.5	0.26246	8.11	1.86	<1.00	0.59	44.302	43.979
074645.05+314149.2	0.32696	7.55	3.31	<1.00	0.54	44.972	43.504
074820.97+340752.6	0.34304	8.09	3.08	<1.00	0.68	44.482	43.986
074948.26+345444.0	0.13181	7.71	1.16	0.82	-0.01	44.129	43.526
075217.84+193542.2	0.11723	9.43	2.59	22.95	0.84	43.173	42.932
075245.60+261735.7	0.08216	6.92	0.46	1.27	0.13	43.924	42.985
075819.68+421935.1	0.21125	7.97	2.84	1.81	0.36	44.958	43.865
075949.54+320023.9	0.18805	7.60	1.92	<1.00	0.35	44.488	43.353
080559.94+260602.3	0.13594	8.31	1.34	<1.00	-0.09	43.371	42.525
080644.65+384318.3	0.34539	7.98	3.28	<1.00	0.71	44.954	44.363
081054.73+501319.5	0.32184	9.13	5.47	<1.00	0.37	44.258	43.940
081317.91+435620.7	0.25455	8.30	1.81	<1.00	0.60	44.351	43.472
081427.69+433705.1	0.22418	7.61	1.27	<1.00	0.47	44.205	43.334
081738.33+242330.0	0.28259	8.20	4.23	4.45	0.86	44.599	44.382
082633.51+074248.4	0.31064	8.14	7.54	<1.00	0.12	44.876	43.978
082640.73+063041.5	0.17092	7.82	0.80	<1.00	0.50	44.165	43.175
083120.99+483154.4	0.33466	7.56	3.30	<1.00	0.62	45.087	44.444
083225.34+370736.1	0.09191	9.22	1.20	11.73	0.75	44.291	43.776
083417.91+491439.2	0.17315	7.40	0.93	<1.00	0.26	44.082	43.225
083443.80+382632.7	0.28822	8.59	2.94	<1.00	0.48	45.016	43.780
083553.46+055317.1	0.20438	7.49	2.24	<1.00	0.15	44.031	43.165
083658.91+442602.4	0.25443	8.74	13.58	10.25	0.64	45.314	44.562
084230.51+495802.3	0.30508	8.53	2.88	<1.00	0.54	44.447	43.552
084504.20+542612.0	0.30317	7.97	1.53	<1.00	0.88	44.427	43.895
084853.09+282411.8	0.19820	8.29	0.81	<1.00	0.60	44.265	43.715
085259.22+031320.6	0.29708	8.31	8.80	<1.00	-0.02	44.334	43.979
085632.39+504114.0	0.23471	8.20	5.11	<1.00	-0.10	44.005	43.129
085828.69+342343.8	0.25666	8.70	6.43	<1.00	-0.08	45.039	43.989
085900.48+383211.6	0.34551	7.73	2.94	<1.00	0.65	45.459	43.663
085915.65+011800.5	0.28206	8.40	3.25	<1.00	0.46	44.582	43.603
090137.99+532051.1	0.16165	7.11	1.05	<1.00	0.25	44.464	43.359
090151.14+103020.4	0.20093	7.92	4.13	<1.00	-0.14	44.572	43.903
090455.00+511444.6	0.22463	8.20	2.55	<1.00	0.10	44.364	43.564
090519.67+440139.1	0.34246	7.50	1.64	<1.00	0.80	44.898	43.344
090654.47+391455.4	0.24067	7.39	1.85	<1.00	0.51	44.593	43.695
090851.25+444611.2	0.32021	8.34	3.66	<1.00	0.42	44.130	43.885
090932.04+503019.6	0.26728	7.56	1.14	<1.00	0.79	43.933	43.046
091010.00+481341.7	0.11700	8.14	0.86	<1.00	0.00	44.297	43.446
091702.38–004417.5	0.32231	8.71	8.21	<1.00	0.15	45.337	44.643
091755.02+053749.7	0.34898	8.43	1.86	<1.00	0.74	44.573	43.461

Table 1 — *Continued.*

Object SDSS	z	$\log(M_{\text{BH}})$ (M_{\odot})	$L_{\text{F}100 \text{\AA}}$ (10^{44} erg s $^{-1}$)	$F_{20 \text{ cm}}$ (mJy)	R_i	$\log(L_{0.1-2.4 \text{ keV}})$ (erg s $^{-1}$)	$\log(L_{2-10 \text{ keV}})$ (erg s $^{-1}$)
(1)	(2)	(3)	(4)	(5)	(6)	(7)	(8)
091955.35+552137.1	0.12295	8.46	2.33	<1.00	-0.38	44.338	43.412
092309.87+453046.4	0.29238	7.63	2.16	<1.00	0.54	44.672	43.779
092554.44+453544.2	0.32948	7.97	3.10	<1.00	0.47	44.534	43.631
092909.79+464424.0	0.23996	8.64	6.15	<1.00	-0.12	43.833	43.103
092933.58+095617.0	0.23194	7.53	0.95	<1.00	0.70	44.199	43.811
093701.04+010543.7	0.05054	6.92	0.30	<1.00	-0.04	43.885	43.308
093939.69+375705.8	0.23127	7.79	2.24	<1.00	0.34	43.739	42.863
094621.27+471131.3	0.23049	7.67	1.37	<1.00	0.50	44.233	43.890
095048.38+392650.5	0.20564	8.41	3.45	<1.00	-0.16	44.807	44.329
095302.64+380145.2	0.27291	8.45	2.60	<1.00	0.45	44.740	43.853
095823.45+065506.5	0.34581	8.30	5.20	<1.00	0.53	44.715	44.356
095833.95+560224.4	0.21639	6.99	0.74	0.83	0.61	44.113	42.926
095915.65+050355.1	0.16230	7.88	1.42	<1.00	0.10	44.040	42.836
095931.67+504449.0	0.14323	7.54	1.12	<1.00	0.02	43.771	42.984
100033.88+104723.7	0.22648	7.99	2.25	2.17	0.29	44.776	43.656
100201.76+620816.3	0.13379	6.98	0.35	<1.00	0.49	44.093	43.173
100420.13+051300.4	0.16049	7.61	2.61	<1.00	-0.12	43.401	42.547
100541.86+433240.4	0.17843	7.79	2.67	2.81	0.47	44.844	43.917
100627.94+603043.6	0.21025	7.15	1.00	<1.00	0.56	44.164	43.081
100744.54+500746.6	0.21204	7.67	2.51	<1.00	0.18	44.594	43.861
101044.51+004331.3	0.17757	8.83	3.15	0.77	-0.36	44.556	43.211
101401.86+461953.7	0.32112	8.38	5.56	<1.00	0.22	44.707	43.696
101415.14+091839.3	0.32524	8.62	1.18	<1.00	0.58	44.500	43.999
101437.46+440639.1	0.20014	7.62	1.38	<1.00	0.31	44.251	43.458
101730.97+470225.0	0.33499	7.91	3.62	<1.00	0.48	44.629	43.732
101852.45+495800.3	0.15481	7.00	0.41	<1.00	0.63	43.931	43.436
102309.48+082602.1	0.34411	8.02	2.69	<1.00	0.60	44.492	43.585
102512.85+480853.2	0.33156	8.50	2.35	<1.00	0.66	44.289	43.386
102531.28+514034.8	0.04488	7.05	0.29	0.60	-0.43	44.038	42.994
102745.84+051558.9	0.31480	7.56	3.02	<1.00	0.45	44.648	43.411
103421.70+605318.1	0.22775	8.07	1.97	<1.00	0.29	44.158	43.292
103457.29-010209.0	0.32801	7.64	3.20	<1.00	0.51	44.791	43.891
104041.50+600239.3	0.29711	7.63	2.53	<1.00	0.54	44.318	43.656
104541.76+520235.5	0.28393	7.87	5.73	<1.00	0.16	44.855	43.895
105007.75+113228.6	0.13344	7.65	2.50	1.50	-0.10	44.264	43.445
105055.14+552723.2	0.33196	7.86	5.20	<1.00	0.33	45.165	44.059
105118.23+605008.2	0.27603	7.98	1.97	<1.00	0.61	44.031	42.963
105444.70+483139.0	0.28651	8.73	10.08	1.56	-0.00	45.219	44.523
105752.69+105037.9	0.22033	7.23	1.20	<1.00	0.48	44.458	43.585
105830.13+601600.3	0.14868	7.56	1.40	<1.00	-0.11	44.300	43.041
110016.19+393524.5	0.31265	7.71	1.60	<1.00	0.88	44.998	43.979
110540.09+064225.7	0.23046	8.36	1.20	<1.00	0.36	44.178	44.159
111006.95+612521.4	0.26234	7.60	1.46	<1.00	0.51	44.403	43.527
111706.39+441333.3	0.14382	8.73	4.02	<1.00	-0.45	43.323	42.475
111740.48+530151.3	0.15851	7.56	0.83	<1.00	0.36	43.783	43.081
111830.28+402554.0	0.15457	7.67	3.16	2.32	0.06	44.670	43.826
112114.21+032546.8	0.15203	7.62	1.12	2.20	0.59	43.858	43.871
112417.79+602026.7	0.20470	7.27	1.06	<1.00	0.49	44.288	43.619
112439.18+420145.0	0.22503	8.18	7.01	<1.00	-0.30	44.623	43.072
112646.43-013417.9	0.34095	8.32	2.30	<1.00	0.80	44.001	43.866
112941.93+512050.6	0.23385	7.47	2.50	1.26	0.36	44.719	43.577
113105.04+610405.0	0.33802	7.95	3.64	<1.00	0.46	44.206	43.415
113422.48+041127.6	0.10800	8.19	1.04	<1.00	-0.26	44.366	43.591
113706.84+013948.0	0.19262	8.73	2.64	<1.00	0.07	44.714	44.322

Table 1 – Continued.

Object SDSS	z	$\log(M_{\text{BH}})$ (M_{\odot})	$L_{\text{F}100 \text{\AA}}$ ($10^{44} \text{ erg s}^{-1}$)	$F_{20 \text{ cm}}$ (mJy)	R_i	$\log(L_{0.1-2.4 \text{ keV}})$ (erg s^{-1})	$\log(L_{2-10 \text{ keV}})$ (erg s^{-1})
(1)	(2)	(3)	(4)	(5)	(6)	(7)	(8)
113738.04+103930.1	0.17454	8.06	2.55	1.65	0.20	44.405	43.707
113908.97+591154.8	0.06127	7.86	0.76	<1.00	-0.48	43.543	43.303
114039.86+414545.9	0.23833	7.87	1.37	<1.00	0.54	44.647	43.770
114105.71+024117.0	0.09313	7.55	0.47	<1.00	0.06	43.623	43.092
114327.21+431145.9	0.30505	8.05	3.38	<1.00	0.44	44.447	43.550
114341.97-014434.5	0.10522	7.52	0.82	<1.00	0.04	43.280	42.444
114408.90+424357.5	0.27248	7.74	2.20	<1.00	0.58	44.499	43.612
114559.00+040409.8	0.27359	7.69	1.31	<1.00	0.88	43.916	43.889
114954.99+044812.9	0.26951	7.53	3.02	1.76	0.62	44.474	43.529
115105.41+445309.3	0.34394	7.35	1.99	<1.00	0.75	44.455	43.548
115507.61+520129.6	0.15399	7.30	1.12	2.05	0.58	43.652	42.801
115549.43+502117.1	0.28443	8.05	3.08	<1.00	0.43	44.386	43.495
115558.97+593129.3	0.24081	7.98	2.25	<1.00	0.36	44.603	43.579
115632.24+112653.7	0.22582	7.52	1.54	<1.00	0.38	44.176	43.302
115758.73-002220.7	0.25984	8.42	3.25	<1.00	0.14	44.034	44.029
120118.43+060024.1	0.33555	8.79	2.16	<1.00	0.64	44.307	43.402
120233.08+022559.7	0.27287	8.51	2.85	<1.00	0.37	44.197	43.366
120347.70+520749.7	0.17760	8.50	4.92	0.68	-0.54	44.681	43.957
121018.35+015405.9	0.21589	8.40	2.71	<1.00	0.22	43.768	43.174
122420.28+435157.9	0.32172	8.44	2.39	<1.00	0.69	44.520	43.880
122549.28+472343.8	0.31883	7.56	2.04	<1.00	0.66	44.294	43.394
123054.12+110011.1	0.23596	8.29	3.67	<1.00	-0.02	44.503	44.301
123115.20+590707.2	0.32605	8.05	3.14	<1.00	0.48	44.461	44.272
123220.11+495721.7	0.26188	7.65	2.94	<1.00	0.50	45.082	43.929
123234.05+092815.2	0.34665	8.33	2.35	<1.00	0.74	44.614	43.812
123958.57+490540.1	0.23550	7.04	1.08	<1.00	0.59	43.941	43.308
124441.41+585626.8	0.19806	7.25	0.75	<1.00	0.54	44.667	43.269
124635.24+022208.7	0.04818	6.75	0.31	2.23	0.25	44.057	43.159
124931.72+523039.2	0.16228	8.00	2.66	<1.00	-0.14	44.447	43.272
125519.69+014412.3	0.34318	8.92	15.52	1.47	0.11	45.350	44.548
125719.56+442935.4	0.30025	8.25	7.68	<1.00	0.00	44.818	44.084
125824.57+540429.8	0.34769	8.12	2.17	<1.00	0.76	44.470	43.562
130250.51+111827.9	0.20284	7.47	1.71	<1.00	0.28	44.424	43.334
130416.99+020537.1	0.22854	7.67	2.04	<1.00	0.27	45.378	43.966
130421.84+560817.0	0.29830	7.82	2.17	<1.00	0.62	44.406	43.823
130604.48+453405.4	0.32709	7.52	2.17	<1.00	0.80	44.683	44.095
131308.67+542115.5	0.29798	8.45	2.90	<1.00	0.63	44.455	43.872
131404.97+153054.2	0.16517	7.94	1.27	<1.00	0.22	44.285	43.363
131651.70+630719.9	0.34724	8.65	2.01	<1.00	0.79	44.110	44.246
132144.96+033055.7	0.26889	8.70	5.48	<1.00	0.02	44.386	43.765
132242.47-022522.0	0.12115	7.69	0.68	<1.00	0.18	43.569	43.592
132447.65+032432.6	0.30578	8.25	4.70	<1.00	0.16	44.358	43.461
132643.62+015209.4	0.19670	7.68	0.85	<1.00	0.52	44.339	43.680
132802.54+441805.3	0.23155	8.13	0.77	<1.00	0.84	43.756	42.880
133051.24+412858.1	0.18174	7.70	1.58	<1.00	0.17	44.429	43.511
133300.83+451809.0	0.31974	8.36	3.65	<1.00	0.37	44.727	44.267
133423.30+434331.7	0.22551	7.65	1.31	<1.00	0.58	44.290	43.751
133636.65+420934.1	0.22328	8.23	2.46	3.55	0.73	43.559	42.685
134032.02+052158.5	0.27448	8.73	2.26	<1.00	0.63	44.668	43.892
134206.57+050523.8	0.26602	7.59	3.48	3.85	0.90	44.468	43.582
134251.60-005345.2	0.32581	8.37	6.22	<1.00	0.26	44.366	43.364
134444.17+630337.2	0.29218	7.80	0.98	<1.00	0.85	44.024	43.327
134459.45-001559.5	0.24490	7.55	1.41	<1.00	0.42	44.472	43.475
134845.44+451809.5	0.27653	8.90	3.42	<1.00	0.34	44.715	43.930

Table 1 – Continued.

Object SDSS	z	$\log(M_{\text{BH}})$ (M_{\odot})	$L_{\text{Ly}\alpha 100 \text{\AA}}$ ($10^{44} \text{ erg s}^{-1}$)	$F_{20 \text{ cm}}$ (mJy)	R_i	$\log(L_{0.1-2.4 \text{ keV}})$ (erg s^{-1})	$\log(L_{2-10 \text{ keV}})$ (erg s^{-1})
(1)	(2)	(3)	(4)	(5)	(6)	(7)	(8)
135829.58+010908.4	0.24392	8.30	1.76	<1.00	0.60	44.118	43.240
135946.91+581357.0	0.22391	7.44	0.68	<1.00	0.70	44.096	43.716
140050.21+532424.5	0.17466	7.25	1.06	<1.00	0.27	43.538	42.678
140104.18+635234.0	0.34386	8.44	3.47	<1.00	0.48	44.223	42.802
140604.25+572956.5	0.32581	8.57	2.44	<1.00	0.67	43.943	43.040
140824.76+543817.7	0.29106	7.63	2.36	<1.00	0.59	44.441	43.548
140827.51+142233.2	0.31766	7.48	1.62	<1.00	0.84	44.628	43.795
141046.46+465802.9	0.33409	7.38	2.99	<1.00	0.65	44.873	43.164
141758.25+360741.4	0.21180	7.62	0.81	<1.00	0.44	44.273	43.558
141942.46+591259.4	0.31988	8.37	1.59	<1.00	0.89	44.012	43.318
142424.22+595300.5	0.13495	8.75	2.28	2.51	0.08	44.091	43.537
142455.53+421407.6	0.31603	8.19	7.32	<1.00	0.17	44.661	43.361
142734.80+352543.4	0.34038	7.49	1.69	<1.00	0.78	44.084	43.177
142748.29+050222.0	0.10608	7.24	1.27	<1.00	-0.26	43.657	42.900
143039.30+493538.9	0.20355	7.82	1.86	<1.00	0.32	44.544	43.403
143204.60+394439.0	0.34848	9.05	9.25	<1.00	0.14	44.063	43.154
143704.12+000705.0	0.14036	7.45	0.61	<1.00	0.44	44.165	43.270
143919.31+551317.8	0.25720	8.52	1.10	<1.00	0.77	44.245	43.807
143940.27+030528.6	0.26856	7.23	1.75	<1.00	0.64	45.053	43.949
144012.76+615633.0	0.27547	7.54	4.46	2.88	0.69	44.860	43.701
144050.76+520445.9	0.31834	7.89	3.73	<1.00	0.46	44.684	43.861
144202.82+433708.7	0.23146	8.18	3.54	<1.00	0.20	44.584	44.196
144302.59+404525.1	0.24615	7.79	3.16	<1.00	0.11	44.231	43.673
144645.93+403505.7	0.26709	8.35	11.37	<1.00	-0.13	44.999	44.073
144751.79+505328.7	0.30565	7.56	1.41	<1.00	0.86	44.068	43.173
145006.93+581456.9	0.31520	7.72	3.93	<1.00	0.33	44.714	43.755
145254.74+395714.6	0.22528	7.31	0.79	<1.00	0.72	43.315	43.261
145307.63+380319.6	0.26191	7.32	1.51	<1.00	0.61	44.695	43.416
145439.39+465309.1	0.31645	8.45	1.95	<1.00	0.58	44.502	44.050
145440.39+455008.5	0.32471	7.92	1.24	<1.00	0.86	44.017	43.115
145817.42+455514.8	0.28575	7.79	3.12	<1.00	0.41	44.669	43.422
145824.46+363119.5	0.24637	7.91	3.86	<1.00	0.20	44.384	43.474
150049.15+343727.1	0.31794	7.52	1.95	<1.00	0.74	44.423	43.423
150114.45+393927.7	0.23072	7.51	1.68	<1.00	0.49	43.950	43.074
150155.24+563731.7	0.34338	7.54	2.78	<1.00	0.56	44.370	42.992
150242.39+395208.5	0.34185	8.19	6.59	<1.00	0.22	44.894	43.976
150437.67+541149.6	0.30519	8.39	3.17	<1.00	0.45	44.154	43.128
151304.56+304204.2	0.34801	8.14	5.25	<1.00	0.25	44.886	43.997
151557.75+302357.1	0.25171	7.60	0.94	<1.00	0.70	44.117	43.235
151940.87+320157.9	0.30132	8.35	2.40	<1.00	0.58	44.558	43.896
152153.81+594020.0	0.28599	8.10	2.41	<1.00	0.52	44.260	44.001
152524.16+523205.7	0.32755	8.28	2.85	<1.00	0.59	44.107	43.125
152628.19-003809.4	0.12333	7.40	0.57	<1.00	0.46	43.696	42.856
153941.49+504255.8	0.20315	7.40	2.32	<1.00	0.14	44.766	43.774
154004.24+355050.1	0.16361	8.16	1.31	<1.00	0.17	43.955	43.126
154344.27-001452.1	0.30189	8.16	3.01	<1.00	0.55	44.512	43.620
154348.62+401324.9	0.31826	8.60	4.93	2.75	0.84	44.885	44.080
155207.18+525347.0	0.33519	8.22	2.50	<1.00	0.65	44.313	43.891
155324.25+490726.9	0.25807	8.19	1.88	<1.00	0.59	44.297	43.414
155328.49+095102.0	0.19174	8.83	3.31	<1.00	-0.04	43.859	42.996
155837.88+282839.0	0.32336	8.54	8.80	<1.00	0.12	45.104	44.163
160518.50+375653.5	0.20087	7.55	1.64	<1.00	0.22	44.229	43.314
161118.82+291932.4	0.29364	8.29	1.68	<1.00	0.74	44.127	43.757
161849.25+442517.2	0.33521	8.46	7.97	3.09	0.63	44.636	44.047

Table 1 — *Continued.*

Object SDSS (1)	z (2)	$\log(M_{\text{BH}})$ (M_{\odot}) (3)	$L_{\text{5100}\text{\AA}}$ (10^{44} erg s $^{-1}$) (4)	$F_{20\text{ cm}}$ (mJy) (5)	R_i (6)	$\log(L_{0.1-2.4\text{ keV}})$ (erg s $^{-1}$) (7)	$\log(L_{2-10\text{ keV}})$ (erg s $^{-1}$) (8)
162607.24+335915.2	0.20453	8.10	5.54	3.74	0.44	44.435	43.243
163111.28+404805.2	0.25751	8.03	2.18	<1.00	0.29	44.789	44.152
163631.58+461704.3	0.25170	7.64	1.55	<1.00	0.52	43.988	43.086
164343.24+405654.3	0.34375	7.04	1.34	<1.00	0.95	43.997	43.089
165338.69+634010.6	0.27897	7.54	1.91	<1.00	0.60	44.215	41.701
165352.82+384542.1	0.32302	7.64	1.74	<1.00	0.80	44.414	43.383
165737.30+604939.3	0.31316	7.67	1.48	<1.00	0.92	43.723	43.004
170231.06+324719.6	0.16333	7.76	4.13	1.52	-0.14	44.858	43.879
170302.88+191033.9	0.29045	7.86	4.44	<1.00	0.38	44.980	44.210
170525.54+194722.7	0.19392	8.42	1.33	<1.00	0.48	44.246	43.436
171013.42+334402.6	0.20749	8.67	5.73	4.60	0.40	44.590	43.730
171207.44+584754.5	0.26925	7.69	1.55	<1.00	0.64	44.551	43.446
171601.93+311213.8	0.11015	7.57	1.76	2.42	-0.06	44.301	43.686
171750.59+581514.0	0.31014	8.37	4.19	<1.00	0.42	44.428	43.708
171850.30+304201.6	0.28176	7.39	2.03	0.64	0.43	44.500	43.400
171902.29+593715.8	0.17852	7.49	1.06	<1.00	0.29	44.129	43.018
172711.81+632241.8	0.21736	9.17	2.71	1.23	0.23	44.482	43.647
173229.44+564811.3	0.30320	7.62	1.87	<1.00	0.67	44.309	43.555
211204.85-063535.2	0.20419	7.75	1.71	<1.00	0.34	44.239	43.890
213818.97+011222.4	0.34409	7.99	3.98	<1.00	0.48	44.584	44.853
215010.52-001000.7	0.33481	8.41	1.90	<1.00	0.80	44.719	43.833
215516.14+003250.8	0.27782	7.62	2.11	<1.00	0.59	44.648	43.498
231250.88+001719.0	0.25704	7.56	2.02	<1.00	0.56	44.201	43.319
233512.68-100040.3	0.24288	7.92	0.50	<1.00	0.83	44.095	43.977

Notes: Col. (1): object name in J2000.0; Col. (2): redshift given by the SDSS spectroscopic pipeline; Col. (3): logarithm of black hole mass; Col. (4): luminosity at 5100Å in units of 10^{44} erg s $^{-1}$; Col. (5): flux density at 20 cm, ‘<1’ represents that the object is not yet detected by FIRST; Col. (6): the radio-loudness; Cols. (7)–(8): X-ray luminosity at 0.1–2.4 keV and 2–10 keV.

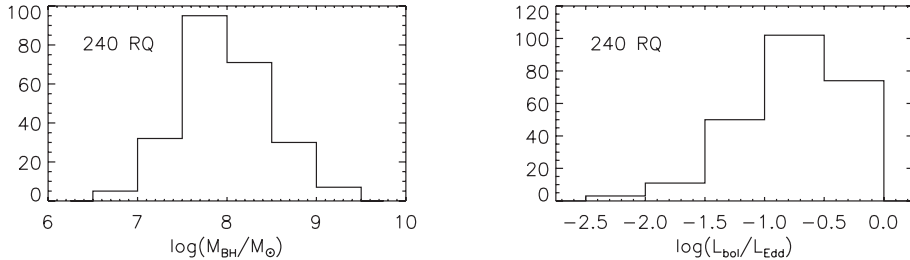


Fig. 1 *Left panel:* the histogram of the black hole masses for our sample. We can see that the center of the distribution of M_{BH} of the RQ sources is nearly $10^{8.0} M_{\odot}$. *Right panel:* the histogram of the Eddington ratio for the sources. Most of the sources show high accretion rates.

its deviation from zero (P_{Null}), representing the probability for randomness of the observed correlation of two variables. Significant correlation of two variables is accepted if P_{null} is less than 0.05. For our sample, the coefficient ρ between $\log(L_{2-10\text{ keV}}/L_{\text{bol}})$ and $\log M_{\text{BH}}$ is 0.001, and P_{Null} is 0.988. This means that the fraction of hard X-rays is independent of black hole mass. For the relation between the hard X-ray fraction and Eddington ratio, we get $\rho = -0.17$ and $P_{\text{Null}} = 0.008$. This indicates that for RQ AGNs, the hard X-ray fraction correlates with the Eddington ratio, and with the increase of the

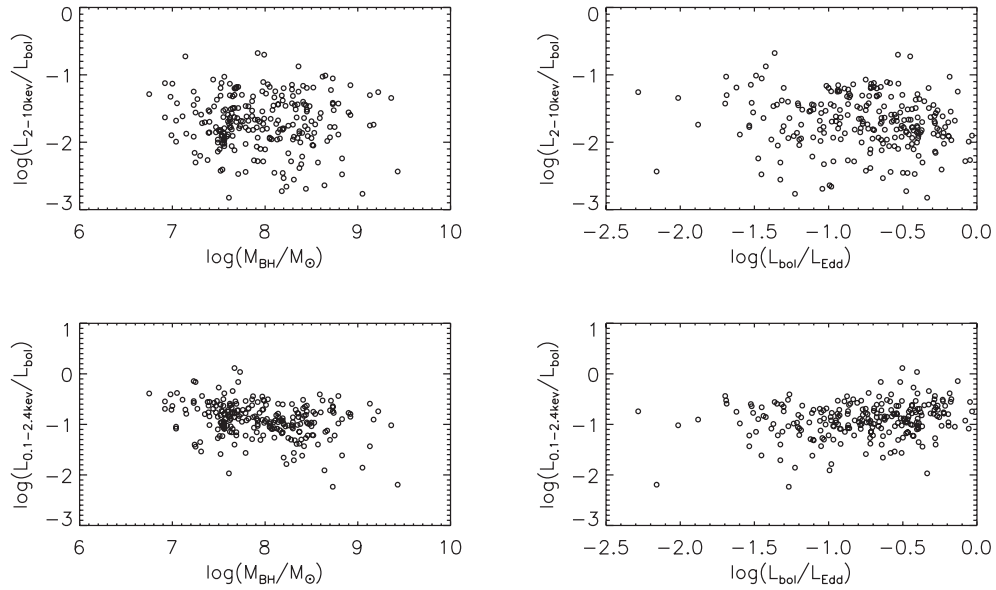


Fig. 2 Fraction of X-ray luminosity in the bolometric luminosity vs. the mass of the black hole and Eddington ratio for our sample. The top panels show how $\log(L_{2-10\text{keV}}/L_{\text{bol}})$ depends on $\log M_{\text{BH}}$ and $\log(L_{\text{bol}}/L_{\text{Edd}})$. The bottom panels describe the trend of $\log(L_{0.1-2.4\text{keV}}/L_{\text{bol}})$ varying with $\log M_{\text{BH}}$ and $\log(L_{\text{bol}}/L_{\text{Edd}})$. We can see that $\log(L_{0.1-2.4\text{keV}}/L_{\text{bol}})$ increases with decrease of the black hole mass and increase of the Eddington ratio.

Eddington ratio, the hard X-ray fraction decreases. This result is qualitatively consistent with the work of Wang et al. (2004).

In addition, we analyze the correlation of the soft X-ray fraction with the black hole mass and Eddington ratio. It is found that the soft X-ray fraction in the bolometric luminosity depends on black hole mass ($\rho = -0.26$, $P_{\text{Null}} = 4.085e-5$), in contrast to the case of hard X-rays. The soft X-ray fraction also positively correlates with the Eddington ratio ($\rho = 0.18$, $P_{\text{Null}} = 0.005$), contrary to the trend of the hard X-ray fraction.

4 INTERPRETATION OF THE CORRELATIONS WITH DISK CORONA MODEL

The hard X-ray radiation from RQ AGNs with a high Eddington ratio is commonly thought to be produced from a disk corona as a result of Comptonization of the softer photons arising from the accretion disk (e.g. Haardt & Maraschi 1993; Kawaguchi et al. 2001; Liu et al. 2003; Cao 2009). If the bolometric luminosity is contributed dominantly by the disk (L_d) and corona (L_c), the fraction of hard X-ray luminosity in the total luminosity represents the strength of the corona relative to the disk. Thus, the negative correlation between the fraction of hard X-rays and the Eddington ratio for RQ AGNs indicates that the corona relative to the disk becomes weaker as the Eddington-scaled accretion rate increases.

Theoretical calculations of radiations from the disk corona (Haardt & Maraschi 1991, 1993) show that the spectral shape does not change with accretion rate. In other words, the ratio (f) of X-ray luminosity and bolometric luminosity is predicted to be independent of the accretion rate. To explain the observational correlation between f and the Eddington accretion rate, Wang et al. (2004), Yang et al. (2007) and Cao (2009) consider magnetic fields and different shear stress tensors. Here we introduce the disk corona evaporation and/or condensation model (Liu et al. 2002b). We show that even without

magnetic fields, the correlation can be simply a consequence of efficient condensation of coronal gas to the disk in the case of high accretion rates.

Assuming that the energy of photons from the disk is amplified by a factor of $A \equiv \Delta\epsilon/\epsilon$ in the process of collisions with electrons when going through the corona, for non-relativistic thermal distributions of electrons, A is a function of electron temperature (T_e) and optical depth (τ_{es}) of the corona,

$$A = \frac{4kT_e}{m_e c^2} \tau_{es}. \quad (5)$$

The fraction of hard X-ray luminosity is expressed as,

$$\frac{L_{2-10 \text{ keV}}}{L_{\text{bol}}} = \frac{AL_d}{AL_d + L_d} = \frac{1}{1 + \frac{1}{A}}. \quad (6)$$

In the case of high accretion rate, disk radiations are strong, which leads to efficient inverse Compton scattering in the corona. As a consequence of over-cooling, part of the coronal gas condenses into the disk, thereby the optical depth decreases and hence the amplification factor is low. The higher the accretion rate is, the lower the density of the corona is. Therefore, from Equation (6), one can see that the fraction of X-rays decreases at high accretion rates. Thus, the negative correlation between the fraction of hard X-ray luminosity and the Eddington ratio can be explained by the coronal condensation to the disk as a consequence of pressure and energy balance between the disk and corona.

Detailed calculations of condensation rate and luminosity have been carried out by Liu et al. (2007) and Taam et al. (2008). In this model, when the Compton scattering is the dominant cooling mechanism, the luminosities from the corona and disk are respectively as follows (Taam et al. 2008),

$$\begin{aligned} L_c &= \int_{3R_s}^{R_{\text{out}}} 2\pi RH \frac{4kT_e}{m_e c^2} n_e \sigma_T 4\sigma T_{\text{eff}}^4(R) dR \\ &= 4.11 \times 10^{38} \alpha^{-\frac{7}{5}} m \dot{m}_c^{\frac{7}{5}} \dot{m}_d^{\frac{3}{5}} \int_3^{r_{\text{out}}} \left(\frac{3}{r}\right)^{\frac{23}{10}} \left[1 - \left(\frac{3}{r}\right)^{\frac{1}{2}}\right]^{\frac{3}{5}} dr. \end{aligned} \quad (7)$$

$$\begin{aligned} L_d &= \int_{3R_s}^{R_{\text{out}}} \sigma T_{\text{eff}}^4(R) 4\pi R dR \\ &= \int_{3R_s}^{R_{\text{out}}} \frac{3GM\dot{M}_d}{8\pi R^3} \left[1 - \left(\frac{3R_s}{R}\right)^{\frac{1}{2}}\right] 4\pi R dR \\ &= 9.38 \times 10^{38} m \dot{m}_d \int_3^{r_{\text{out}}} \frac{1}{r^2} \left[1 - \left(\frac{3}{r}\right)^{\frac{1}{2}}\right] dr. \end{aligned} \quad (8)$$

where $r = R/R_s$ (R_s represents the Schwarzschild radius), $m = M_{\text{BH}}/M_\odot$, \dot{m}_c is the Eddington-scaled accretion rate in the corona and \dot{m}_d the one in the disk. Note that for a truncated inner disk lying under a corona, \dot{m}_d comes only from the condensation of coronal gas; while in the case of a full disk coexisting with a corona for AGNs discussed here, the accretion rate in the disk is mainly from the outer region, $\dot{m}_d = \dot{m} - \dot{m}_c$. We then derive the ratio of coronal luminosity to disk luminosity,

$$L_c/L_d \propto \alpha^{-\frac{7}{5}} \dot{m}_c^{\frac{7}{5}} \dot{m}_d^{-\frac{2}{5}} = \alpha^{-\frac{7}{5}} \dot{m}_c^{\frac{7}{5}} (\dot{m} - \dot{m}_c)^{-\frac{2}{5}}. \quad (9)$$

In the disk corona evaporation and/or condensation model, the coronal accretion flow is supplied by disk evaporation in the region around $300 R_s$. The coronal flow rate \dot{m}_c can be as high as a few percent of the Eddington value if the accretion rate exceeds a few percent of the Eddington value. However, the coronal flow can partially condense into the disk in the inner region as a result of Compton cooling, and the condensation rate is larger at a higher accretion rate. This means that the coronal flow (\dot{m}_c) is lower at a higher accretion rate. From Equation (9), one can see that the ratio of coronal luminosity to

disk luminosity decreases with increasing accretion rate \dot{m} . Noting that the accretion rate in units of Eddington value is equal to the Eddington ratio, the disk corona evaporation and condensation model predicts that the ratio of X-ray luminosity to disk luminosity decreases with increasing Eddington ratio, which can explain the correlation obtained from our RQ AGN sample.

If magnetic fields are also taken into account as an additional heating method (Liu et al. 2003; Cao 2009), the coronal accretion flow can be higher and the corona can be stronger than that without magnetic fields. However, the trend that condensation is stronger at higher accretion rates does not change with the magnetic fields. Therefore, the variation of relative strength of the disk and corona with accretion rates keeps the same trend. Thus, with inclusion of magnetic fields, the model will still work in interpreting the correlations.

Another important feature of the disk corona evaporation and condensation model is that the coronal structure and evaporation/condensation properties are independent of the mass of the black hole if scaled properly. In fact, the model can be applied in both X-ray binaries and AGNs. Equation (9) shows that the luminosity ratio from the corona and the disk indeed does not vary with the mass of the black hole. Therefore, the model can explain why for our sample the fraction of hard X-ray luminosity is independent of the mass of the black hole.

5 DISCUSSION

5.1 Implication to the Hard X-ray Bolometric Correction

The bolometric luminosity is either estimated from the measured luminosity at 5100 Å or from hard X-ray luminosity with fixed correction factors. However, our data analysis shows that the hard X-ray fraction in the bolometric luminosity decreases with increasing Eddington ratio for RQ AGNs. This means that the bolometric correction factor from hard X-rays, $k_{2-10\text{ keV}} = L_{\text{bol}}/L_{2-10\text{ keV}}$, should increase with an increasing Eddington ratio. This result is in good agreement with that of Vasudevan & Fabian (2007), which is drawn from 54 AGNs with available SEDs. Note that in our study, we calculate the bolometric luminosity from $9\lambda L_\lambda$ (5100 Å). If the bolometric correction factor for $L_{5100\text{ \AA}}$ also tends to increase with Eddington ratio (see fig. 15 of Vasudevan & Fabian 2007), the hard X-ray fraction in bolometric luminosity would be even smaller at higher Eddington ratios for our sample. Therefore, our statistical results support that the bolometric correction for hard X-rays increases with an increasing Eddington ratio.

5.2 The Constant Photon Index

In order to investigate the strength of the corona, i.e. to get the hard X-ray flux, we use the same photon indices for all objects in our sample to extrapolate the hard X-ray emission from 2 keV flux. From the above analysis, we get a smaller absolute coefficient value (ρ) between the fraction of hard X-ray luminosity and the Eddington ratio. However, if we note that for some individual objects, the spectra become softer when a source is brighter (e.g., Lu & Yu 1999; Bian 2005; Middleton et al. 2008; Saez et al. 2008) and this effect is taken into account, the hard X-ray luminosity fraction should change with the Eddington ratio more steeply than our results since here we assume the photon index is constant when calculating the hard X-ray luminosity.

5.3 The Origin of Soft X-rays in 0.1–2.4 keV

Our study also indicates that for the same RQ AGNs, the fraction of soft X-ray luminosity in the ROSAT energy band (0.1 – 2.4 keV) anticorrelates with the mass of the black hole, as shown in Figure 2. If the soft X-rays are also from the corona, the correlation should be similar to that for hard X-rays, that is, the fraction of soft X-rays is independent of the black hole mass. On the other hand, if the disk emits dominantly in soft X-rays, the fraction of soft X-rays to the total luminosity should also be independent of the mass of the black hole since both the total luminosity and disk luminosity are proportional to the

mass of the black hole. We note that the effective temperature of the disk decreases with the mass of the black hole (e.g., Thorne 1974; Bonning et al. 2007), $\sigma T_{\text{eff}}^4 = \frac{3GM\dot{M}}{8\pi R^3} [1 - (3R_s/R)^{1/2}]$, reaching a maximum at $R = (49/36)(3R_s)$ (see Liu et al. 2007),

$$T_{\text{eff},\text{max}} = 1.3 \times 10^5 (M_{\text{BH}}/10^8 M_{\odot})^{-1/4} \dot{m}^{1/4} \text{ K.} \quad (10)$$

For an AGN with a high mass black hole, the disk does not emit in soft X-rays but rather in the optical/UV band. With mass decrease, the high energy part of the disk spectrum could extend to soft X-rays. Consequently, the fraction of disk contribution to the soft X-ray component increases with the decrease of M_{BH} . This could lead to a negative correlation between the fraction of soft X-rays and the mass of the black hole, qualitatively consistent with the observational results shown in Section 3. Therefore, the different correlations with black hole mass of the soft X-rays and hard X-rays may indicate that the soft X-rays are not only contributed from the corona but also the disk. Zhou et al. (1997) separated two components in the soft X-ray region through statistically analyzing the Big Blue Bump.

6 CONCLUSIONS

We compile a blue AGN sample containing Seyfert 1 galaxies and QSOs with 240 AGNs being RQ. We mainly investigate the dependence of the fraction of hard X-ray luminosity in bolometric luminosity ($\log(L_{2-10\text{ keV}}/L_{\text{bol}})$) on the black hole mass and Eddington ratio in RQ AGNs by using Spearman's rank correlation. We find that the fraction of hard X-ray luminosity in bolometric luminosity decreases with the increase of the Eddington ratio for RQ AGNs, while the fraction of hard X-ray luminosity in the bolometric luminosity is independent of the black hole mass for a wide range of black hole masses. The correlation between the hard X-ray and bolometric luminosity suggests that the hard X-ray bolometric correction increases at high Eddington ratios, confirming Vasudevan & Fabian (2007)'s results from a larger sample. These observational features support the disk corona model developed by Meyer et al. (2000) and Liu et al. (2002b). Combining the theoretical model and the wide range of black hole masses in our sample, we suggest that the intrinsic accretion processes in AGNs and black hole X-ray binaries are similar.

Acknowledgements We are grateful to the anonymous referee for constructive and enlightening comments. Liu J. Y. greatly thanks Yuan W. for instruction on X-ray data reduction and statistical analysis. We also acknowledge Dong X. B. for the SDSS data analysis. This work is supported by the National Natural Science Foundation of China (Grant Nos. 10533050 and 10773028) and the National Basic Research Program of China-973 Program 2009CB824800.

References

- Bian, W. H. 2005, ChJAA (Chin. J. Astron. Astrophys.), 5S, 289
- Bisnovatyi-Kogan, G. S., & Blinnikov, S. I. 1976, SvAL, 2, 191
- Bonning, E. W., Cheng, L., et al. 2007, ApJ, 659, 211
- Cao, X. W. 2009, MNRAS, 394, 207
- Dong, X. B., Wang, T. G., et al. 2008, MNRAS, 383, 581(Dong08)
- Elvis, M., et al. 1994, ApJS, 95, 1
- Galeev, A. A., Rosner, R., & Vaiana, G. S. 1979, ApJ, 229, 318
- Haardt, F., & Maraschi, L. 1991, ApJ, 380, L51
- Haardt, F., & Maraschi, L. 1993, ApJ, 413, 507
- Ivezic, Z., et al. 2002, AJ, 124, 2364
- Kawaguchi, T., Shimura, T., & Mineshige, S. 2001, ApJ, 546, 966
- Liang, E. P. T., & Price, R. H. 1977, ApJ, 218, 247
- Liu, B. F., Yuan, W., Meyer, F., et al. 1999, ApJ, 527, L17
- Liu, B. F., Mineshige, S., & Shibata, K. 2002a, ApJ, 572, L173
- Liu, B. F., Mineshige, S., Meyer, F., et al. 2002b, ApJ, 575, 117

- Liu, B. F., Mineshige, S., & Ohsuga, K. 2003, ApJ, 587, 571
 Liu, B. F., Taam R. E., Meyer-Hofmeister, E., & Meyer, F. 2007, ApJ, 671, 695
 Lu, Y., & Yu, Q. 1999, ApJ, 526, L5
 Lynden-Bell, D., & Pringle, J. E. 1974, MNRAS, 168, 603
 Meyer, F., & Meyer-Hofmeister, E. 1994, A&A, 288, 175
 Meyer, F., Liu, B. F., et al. 2000, A&A, 361, 175
 Middleton, M., Done, C., & Schurch, N. 2008, MNRAS, 383, 1501
 Nakamura, K., & Osaki, Y. 1993, PASJ, 45, 775
 Narayan, R., & Yi, I. 1994, ApJ, 428, L13
 Narayan, R., & Yi, I. 1995, ApJ, 452, 710
 Narayan, R., Mahadevan, R., & Quataert, E. 1998, in The Theory of Black Hole Accretion Discs, eds. M. A. Abramowicz, G. Bjornsson, & J. E. Pringle (Cambridge: Cambridge University Press)
 Peterson, B. M. 1993, PASP, 105, 247
 Peterson, B. M., Ferrarese, L., et al. 2004, ApJ, 613, 682
 Pounds, K. A., Nandra, K., Stewart, G. C., et al. 1990, Nature, 344, 132
 Reeves, J. N., & Turner, M. J. L. 2000, MNRAS, 316, 234
 Saez, C., Chartas, G., et al. 2008, AJ, 135, 1505
 Shakura, N. I., & Sunyaev, R. A. 1973, A&A, 24, 337
 Stella, L., & Rosner, R. 1984, ApJ, 277, 312
 Svensson, R., & Zdziarski, A. A. 1994, ApJ, 436, 599
 Taam, R. E., Liu, B. F., et al. 2008, ApJ, 688, 527
 Thorne, K. S. 1974, ApJ, 191, 507
 Vasudevan, R. V., & Fibian, A. C. 2007, MNRAS, 381, 1235
 Vestergaard, M., & Peterson, B. M. 2006, ApJ, 641, 689
 Voges, W., Gruber, R., Haberl, F., et al. 1994, ROSAT NEWS No.32
 Wang, J. M., Watarai, K. Y., & Mineshige, S. 2004, ApJ, 607, L107
 William, H. P., Saul, A. T., et al. 1992, Numerical Recipes in Fortran (2nd, Cambridge: Cambridge University Press)
 Woo, J. H., & Urry, C. M. 2002, ApJ, 579, 530
 Yang, F., Hu, C., et al. 2007, ChJAA (Chin. J. Astron. Astrophys.), 7, 353
 Zhou, Y. Y., Yu, K. N., et al. 1997, ApJ, 475, L9